Nanoscale Advances

ROYAL SOCIETY OF CHEMISTRY

PAPER

View Article Online
View Journal | View Issue

Cite this: *Nanoscale Adv.*, 2025, **7**, 8154

Estimation of effective anisotropy constant distribution of magnetic nanoparticles based on magnetic particle spectroscopy

Haochen Zhang, *[a] Yi Sun, [a] Haozhe Wang,[a] Zhongzhou Du,[b] Teruyoshi Sasayama[a] and Takashi Yoshida[a]

Magnetic nanoparticles (MNPs) have gained significant attention in biomedical applications such as magnetic particle imaging (MPI) and magnetic hyperthermia. The AC magnetization properties of MNPs, which are crucial for their performance, are influenced by factors such as the core size distribution, saturation magnetization, and effective anisotropy constant. In this study, we proposed a method to estimate an effective anisotropy constant distribution in a MNP sample, which is generally treated as a constant value. Experimental results of the AC magnetization for different MNP samples, including single-core and multi-core samples, were well described by the numerical simulation results in which the estimated effective anisotropy constant distribution was taken into consideration. Furthermore, we demonstrated that the effective anisotropy constant distribution obtained from 1–20 kHz harmonics of AC magnetization measured by magnetic particle spectroscopy (MPS) could be effectively applied to simulations at frequencies up to 40 kHz within 20% relative error, potentially extending the practical frequency range of MPS through simulations. Our findings provide a reliable approach for estimating an effective anisotropy constant distribution in a nano-sized magnetic particle sample, analyzing the AC magnetization properties of MNPs, and optimizing their applications in biomedical fields.

Received 4th July 2025
Accepted 2nd November 2025

DOI: 10.1039/d5na00654f

rsc.li/nanoscale-advances

Introduction

Magnetic nanoparticles (MNPs), a class of biocompatible nanomaterials, have attracted considerable attention due to their promising potential in a wide range of biomedical applications, including magnetic particle imaging (MPI) and magnetic hyperthermia.[1–4] Their AC magnetization properties such as hysteresis loss and higher-order harmonic components play a crucial role in determining their performance in these applications.[5–9] A deep understanding of these AC magnetization properties is therefore essential for the rational design and optimization of MNPs for specific diagnostic and therapeutic purposes. The AC magnetization properties of MNPs are influenced by several factors, including the particle size distribution, saturation magnetization, and effective anisotropy constant. The AC magnetization properties of MNPs can be analysed through both experiments and simulations. Experimentally, the AC M–H curve is measured using magnetic particle spectroscopy (MPS), which is a versatile tool for characterizing MNPs.[10–12] The AC M–H curve can also be obtained through numerical simulation using the Fokker–Planck equation or the stochastic Landau–Lifshitz–Gilbert (LLG) equation,[13–17] under the conditions of known particle size distribution, saturation magnetization, and effective anisotropy constant.

To evaluate and optimize the MNP sample for specific biomedical applications, estimation methods of particle size distribution, saturation magnetization, and the effective anisotropy constant were proposed. Particle size distribution and saturation magnetization can be measured and estimated from a static M–H curve of a MNP sample measured by using a vibrating sample magnetometer (VSM).[18]

Magnetic anisotropy is a key factor governing the dynamic magnetization behavior of nanoparticles. The total effective anisotropy arises from several sources: magnetocrystalline anisotropy, shape anisotropy, and surface anisotropy. In addition, interparticle dipolar interactions may further modify the anisotropy by introducing collective effects. By measuring the coercive field of the MNP sample, and using empirical expressions, the effective anisotropy constant of the entire MNP sample can be estimated.[19–21] Another widely used approach for estimating the effective anisotropy constant of an entire MNP sample is based on the analysis of the blocking temperature derived from zero-field-cooled (ZFC) and field-cooled (FC) magnetization curves.[22,23]

These methods for estimating the effective anisotropy constant can only determine the effective anisotropy constant of the entire MNP sample. As shown later in this paper, however, adjusting the anisotropy constant of the entire MNP sample in

[a]*Department of Electrical and Electronic Engineering, Kyushu University, Fukuoka, Japan. E-mail: zhang.haochen.048@s.kyushu-u.ac.jp*
[b]*School of Computer and Communication Engineering, Zhengzhou University of Light Industry, Zhengzhou, China*

the simulation of the AC M–H curve fails to achieve good agreement with the experimental value. The discrepancy between the experiment and simulation results will be due to the usage of a single value of the effective anisotropy constant K_{eff} in a MNP sample.

In this paper, we propose a method to estimate a K_{eff} distribution under an assumption that it distributes in a MNP sample. The effective anisotropy constant distribution of the MNP sample is derived through non-negative least squares (NNLS) by fitting simulation results of the harmonic magnetizations of MNPs under AC excitation fields with experimental ones. When the estimated K_{eff} distribution was used instead of the single value of K_{eff}, the simulation results closely matched the experimental ones. Furthermore, the K_{eff} distribution of the MNP sample estimated at the excitation field frequencies of 1–20 kHz is sufficient to simulate the AC M–H curves of the MNP sample at frequencies of up to at least 40 kHz.

Experimental materials

Materials

For experiments, commercial single-core MNP samples, SHP-15, SHP-20, and SHP-25 (Ocean NanoTech) each with an iron concentration of 5 mg ml^{-1} were used as sample materials. Additionally, a multi-core MNP sample, called Resovist (neo CritiCare Phama Co., Ltd) with an iron concentration of 27.875 mg ml^{-1} was prepared.

Immobilized MNP samples with easy axis alignment

All samples are immobilized by epoxy resin. We use epoxy resin to fix 10 μl of sample solution. After evenly stirring, the mixed solution was liquid and began to solidify after about 20 min. The sample completely solidified after about 5 h. Until completely solidified, the mixed solution was under a DC field ($\mu_0 H_{\mathrm{dc}} = 1T$) to immobilize the easy axis along the magnetic field direction. After completely solidification, the samples were left for 12 h to evaporate the water. The iron concentration of the SHP series used in the measurement was 0.3 μg μl^{-1}, and that of the Resovist sample was 1.85 μg μl^{-1}.

Methods

Estimation of effective anisotropy constant K_{eff} distribution

When the MNPs are immobilized, the magnetization of MNPs is determined by using the effective anisotropy constant K_{eff}, and core size d_{c}. Employing the superposition model as in the case of suspended MNPs,[24,25] the magnetization M is given by:

$$M = \frac{1}{V_{\mathrm{T}}}\int_0^\infty \int_0^\infty n(d_{\mathrm{c}}, K_{\mathrm{eff}})\, V_{\mathrm{c}} M(d_{\mathrm{c}}, K_{\mathrm{eff}})\, \mathrm{d}\, d_{\mathrm{c}} \mathrm{d}\, K \tag{1}$$

Here, $n(d_{\mathrm{c}},K_{\mathrm{eff}})$ is the number density of MNPs having a core size d_{c} and an effective anisotropy constant K_{eff}, V_{c} is the core volume of MNPs, and V_{T} is the total core volume of MNPs. The dipolar interaction between MNPs is neglected, and the multi-core is approximated as an effective single core in this model.[26]

Discretizing eqn (1) with respect to d_{c} and K_{eff}, M can be rewritten as:

$$M = \frac{1}{V_{\mathrm{T}}}\sum_{j=1}^{J}\sum_{i=1}^{I} n(d_{\mathrm{c}}^{\,j}, K_{\mathrm{eff}}^{\,i})\, V_{c}^{\,j} M(d_{\mathrm{c}}^{\,j}, K_{\mathrm{eff}}^{\,i}) \Delta K^{i} \Delta d_{\mathrm{c}}^{\,j} \tag{2}$$

where I and J denote the sampling numbers for K_{eff} and d_{c}, respectively. By performing Fourier transforms of eqn (2), the k-th harmonic magnetization M_{k} is given by

$$M_k = \sum_{j=1}^{J}\sum_{i=1}^{I} n_{\mathrm{V}}(d_{\mathrm{c}}^{\,j}, K_{\mathrm{eff}}^{\,i})\, M_k(d_{\mathrm{c}}^{\,j}, K_{\mathrm{eff}}^{\,i}) \Delta K^{i} \Delta d_{\mathrm{c}}^{\,j} \tag{3}$$

$$n_{\mathrm{V}}(d_{\mathrm{c}}^{\,j}, K_{\mathrm{eff}}^{\,i}) = \frac{1}{V_{\mathrm{T}}} n(d_{\mathrm{c}}^{\,j}, K_{\mathrm{eff}}^{\,i}) d_{\mathrm{c}}^{\,j} \tag{4}$$

Here, $n_{\mathrm{V}}(d_{\mathrm{c}}^{\,j},K_{\mathrm{eff}}^{\,i})$ represents the volume-weighted number density of MNPs having $d_{\mathrm{c}}^{\,j}$ and $K_{\mathrm{eff}}^{\,i}$. Eqn (3) is the fundamental equation to estimate the K_{eff} distribution. In short, $n_{\mathrm{V}}(d_{\mathrm{c}}^{\,j},K_{\mathrm{eff}}^{\,i})$ is estimated from the experimentally measured M_k and numerically simulated $M_k(d_{\mathrm{c}}^{\,j},K_{\mathrm{eff}}^{\,i})$.

The detailed procedures are follows. The first $M_{1,f}$ and the third $M_{3,f}$ harmonics of magnetization are experimentally measured by using a homebuilt magnetic particle spectrometer (MPS)[27] under an excitation field amplitude of 10 mT and a frequency of f. f is changed in the range of 1–20 kHz with an interval of 1 kHz and $M_{1,f}$ and $M_{3,f}$ for all f are used as the experimental data. On the other hand, the first $M_{1,f}(d_{\mathrm{c}}^{\,j},K_{\mathrm{eff}}^{\,i})$ and the third $M_{3,f}(d_{\mathrm{c}}^{\,j},K_{\mathrm{eff}}^{\,i})$ harmonics of magnetization of MNPs having $d_{\mathrm{c}}^{\,j}$ and $K_{\mathrm{eff}}^{\,i}$ are numerically simulated based on the Fokker–Plank equation[28] and used as the simulation data. Using the experimental and simulation data, eqn (3) is rewritten as

$$\boldsymbol{M}_{\mathrm{exp}} = \boldsymbol{M}_{\mathrm{sim}}\boldsymbol{P} \tag{5}$$

Here, each matrix is given by eqn (6)–(8) and subscripts of "exp" and "sim" represent experimental and simulation data, respectively.

$$\boldsymbol{M}_{\mathrm{exp}} = [M_{1,\mathrm{exp},1\mathrm{kHz}} \cdots M_{1,\mathrm{exp},20\mathrm{kHz}} M_{3,\mathrm{exp},1\mathrm{kHz}} \cdots M_{3,\mathrm{exp},20\mathrm{kHz}}]^{T} \tag{6}$$

$$\boldsymbol{P} = [n_{\mathrm{V}}(d_{\mathrm{c}}^{\,1},K_{\mathrm{eff}}^{\,1})\Delta K^{1}\Delta d_{\mathrm{c}}^{\,1} \cdots n_{\mathrm{V}}(d_{\mathrm{c}}^{\,1},K_{\mathrm{eff}}^{\,I})\Delta K^{\mathrm{I}}\Delta d_{\mathrm{c}}^{\,1} \cdots n_{\mathrm{V}}(d_{\mathrm{c}}^{\,J},K_{\mathrm{eff}}^{\,1}) \Delta K^{1}\Delta d_{\mathrm{c}}^{\,J} \cdots n_{\mathrm{V}}(d_{\mathrm{c}}^{\,J},K_{\mathrm{eff}}^{\,I})\Delta K^{\mathrm{I}}\Delta d_{\mathrm{c}}^{\,J}]^{T} \tag{7}$$

$$\boldsymbol{M}_{\mathrm{sim}} = \begin{bmatrix} M_{1,\mathrm{sim},1\mathrm{kHz}}(d_{\mathrm{c}}^{\,1},K_{\mathrm{eff}}^{\,1}) & \cdots & M_{1,\mathrm{sim},1\mathrm{kHz}}(d_{\mathrm{c}}^{\,J},K_{\mathrm{eff}}^{\,1}) & \cdots & M_{1,\mathrm{sim},1\mathrm{kHz}}(d_{\mathrm{c}}^{\,J},K_{\mathrm{eff}}^{\,1}) & \cdots & M_{1,\mathrm{sim},1\mathrm{kHz}}(d_{\mathrm{c}}^{\,J},K_{\mathrm{eff}}^{\,1}) \\ \vdots & \ddots & \vdots & \ddots & \vdots & \ddots & \vdots \\ M_{1,\mathrm{sim},20\mathrm{kHz}}(d_{\mathrm{c}}^{\,1},K_{\mathrm{eff}}^{\,1}) & \cdots & M_{1,\mathrm{sim},20\mathrm{kHz}}(d_{\mathrm{c}}^{\,1},K_{\mathrm{eff}}^{\,1}) & \cdots & M_{1,\mathrm{sim},20\mathrm{kHz}}(d_{\mathrm{c}}^{\,J},K_{\mathrm{eff}}^{\,1}) & \cdots & M_{1,\mathrm{sim},20\mathrm{kHz}}(d_{\mathrm{c}}^{\,J},K_{\mathrm{eff}}^{\,1}) \\ M_{3,\mathrm{sim},1\mathrm{kHz}}(d_{\mathrm{c}}^{\,1},K_{\mathrm{eff}}^{\,1}) & \cdots & M_{3,\mathrm{sim},1\mathrm{kHz}}(d_{\mathrm{c}}^{\,1},K_{\mathrm{eff}}^{\,1}) & \cdots & M_{3,\mathrm{sim},1\mathrm{kHz}}(d_{\mathrm{c}}^{\,J},K_{\mathrm{eff}}^{\,1}) & \cdots & M_{3,\mathrm{sim},1\mathrm{kHz}}(d_{\mathrm{c}}^{\,J},K_{\mathrm{eff}}^{\,1}) \\ \vdots & \ddots & \vdots & \ddots & \vdots & \ddots & \vdots \\ M_{3,\mathrm{sim},20\mathrm{kHz}}(d_{\mathrm{c}}^{\,1},K_{\mathrm{eff}}^{\,1}) & \cdots & M_{3,\mathrm{sim},20\mathrm{kHz}}(d_{\mathrm{c}}^{\,1},K_{\mathrm{eff}}^{\,1}) & \cdots & M_{3,\mathrm{sim},20\mathrm{kHz}}(d_{\mathrm{c}}^{\,J},K_{\mathrm{eff}}^{\,1}) & \cdots & M_{3,\mathrm{sim},20\mathrm{kHz}}(d_{\mathrm{c}}^{\,J},K_{\mathrm{eff}}^{\,1}) \end{bmatrix} \tag{8}$$

Then, the $\boldsymbol{P}$ vector is estimated from the $\boldsymbol{M}_{\mathrm{exp}}$ vector and $\boldsymbol{M}_{\mathrm{sim}}$ matrix by solving eqn (5) using a non-negative least squares (NNLS) method under a constraint of eqn (9).

$$\sum_{i=1}^{I} n_{\mathrm{V}}\left(d_{\mathrm{c}}^{j}, {K_{\mathrm{eff}}}^{i}\right)\Delta K^{i} = n_{d_{\mathrm{c,V}}}\left(d_{\mathrm{c}}^{j}\right) \quad (\text{for } j = 1 \text{ to } J) \tag{9}$$

Here, $n_{d_{\mathrm{c,V}}}(d_{\mathrm{c}}^{j})$ represents the volume-weighted number density of MNPs having d_{c}^{j}, which is obtained from a static M–H curve. Details of obtaining $n_{d_{\mathrm{c,V}}}(d_{\mathrm{c}}^{j})$ are provided in the supplementary file.

Simulation method

In these numerical simulations, only Néel relaxation is considered and the effect of dipolar interaction is neglected. Additionally, the easy axis of MNPs is fixed in the magnetic field direction. To compare the experimentally measured M–H curve with the simulated one, the parameters of the AC excitation magnetic field in the numerical simulation were set to be consistent with those used in the experiment.

Results

AC M–H curve

The measured AC M–H curves of the SHP-20 sample for different excitation frequencies are shown in Fig. 1. The calculated AC M–H curves using a single-valued K_{eff}, which are given by using eqn (10), are also shown in Fig. 1.

$$M = \sum_{j=1}^{J} n_{d_{\mathrm{c,V}}}\left(d_{\mathrm{c}}^{j}\right) M_{\mathrm{LLG}}\left(d_{\mathrm{c}}^{j}, K_{\mathrm{eff}}\right)\Delta d_{\mathrm{c}}^{j} \tag{10}$$

Here, M_{LLG} was numerically calculated from the stochastic Landau–Lifshitz–Gilbert (LLG) equation. Details of the simulation procedure are provided elsewhere.[29] As can be seen from Fig. 1, it was found that the calculated AC M–H curves using a single-valued K_{eff} cannot explain the experimental ones. The same applies to the other samples as shown in Fig. S8. This indicates that the value of K_{eff} was distributed in each MNP sample examined.

Anisotropy constant K_{eff} distribution

Fig. 2 shows the distribution of K_{eff} for the SHP-20 sample, which is estimated from eqn (5)–(9). Here P_{n} represents the normalized volume-weighted number of MNPs with core diameter d_{c}^{j} and ${K_{\mathrm{eff}}}^{j}$, which is given by:

$$P_{\mathrm{n}}\left(d_{\mathrm{c}}^{j}, {K_{\mathrm{eff}}}^{i}\right) = \frac{n_{\mathrm{V}}\left(d_{\mathrm{c}}^{j}, {K_{\mathrm{eff}}}^{i}\right)\Delta K^{i}\Delta d_{\mathrm{c}}^{j}}{\sum_{i=1}^{I} n_{\mathrm{V}}\left(d_{\mathrm{c}}^{j}, {K_{\mathrm{eff}}}^{i}\right)\Delta K^{i}\Delta d_{\mathrm{c}}^{j}} \tag{11}$$

As can be seen, K_{eff} for each d_{c}^{j} is narrowly distributed. Therefore, it is reasonable to represent K_{eff} for d_{c}^{j} with a single value. Here, a parameter of an effective anisotropy constant as a function of d_{c}^{j} is introduced as follows:

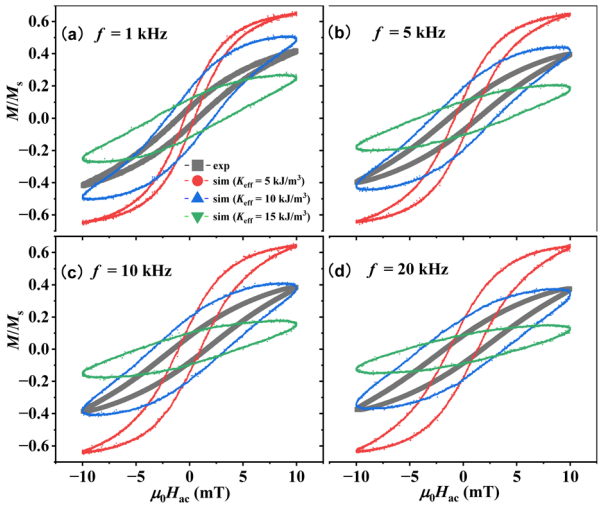

Fig. 1 Comparison between the experimental and simulation results of AC M–H for the SHP-20 sample under an excitation field amplitude of $\mu_0 H_{\mathrm{ac}} = 10$ mT and a frequency of (a) 1 kHz, (b) 5 kHz, (c) 10 kHz, and (d) 20 kHz, respectively. In the simulations, the effective anisotropy constant $K_{\mathrm{eff}}(d_{\mathrm{c}}^{j})$ is set to a constant value in the SHP-20 sample and changed from 5–15 kJ m^{-3}.

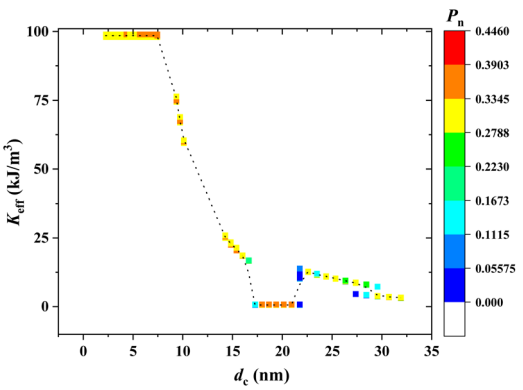

Fig. 2 Distribution of K_{eff} on d_{c} of the SHP-20 sample. P_{n} is the normalized volume-weighted number of MNPs with core diameter d_{c}^{j} and ${K_{\mathrm{eff}}}^{j}$. A dotted line is added to guide the eye.

$$K_{\mathrm{eff}}\left(d_{\mathrm{c}}^{j}\right) = \frac{\sum_{i=1}^{I} {K_{\mathrm{eff}}}^{i} n_{\mathrm{V}}\left(d_{\mathrm{c}}^{j}, {K_{\mathrm{eff}}}^{i}\right)\Delta K^{i}}{\sum_{i=1}^{I} n_{\mathrm{V}}\left(d_{\mathrm{c}}^{j}, {K_{\mathrm{eff}}}^{i}\right)\Delta K^{i}} \tag{12}$$

To verify the accuracy of $K_{\mathrm{eff}}(d_{\mathrm{c}}^{j})$, which is given by using eqn (12) and shown in Fig. 2, the AC M–H curves were reconstructed by incorporating the $K_{\mathrm{eff}}(d_{\mathrm{c}}^{j})$ distribution into the calculation given by:

$$M = \sum_{j=1}^{J} n_{d_{\mathrm{c,V}}}\left(d_{\mathrm{c}}^{j}\right) M_{\mathrm{LLG}}\left(d_{\mathrm{c}}^{j}, K_{\mathrm{eff}}\left(d_{\mathrm{c}}^{j}\right)\right)\Delta d_{\mathrm{c}}^{j} \tag{13}$$

Fig. 3 shows the comparison of the AC M–H curves of the SHP-20 sample between the measured and simulated curves

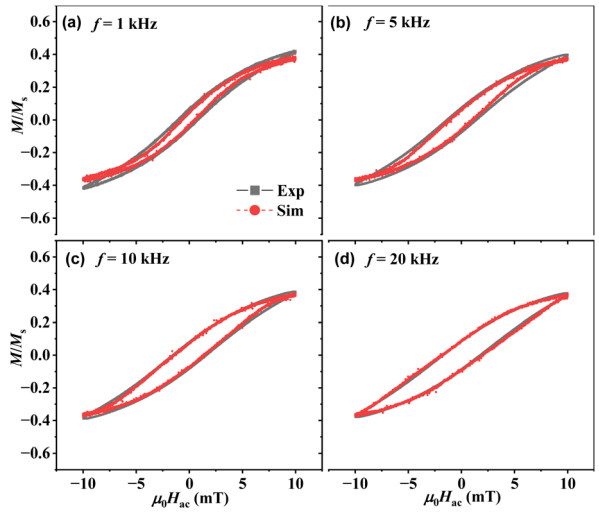

Fig. 3 Comparison between the experimental and simulation results of AC M–H for the SHP-20 sample under an excitation field amplitude of $\mu_0 H_{ac} = 10$ mT and a frequency of (a) 1 kHz, (b) 5 kHz, (c) 10 kHz, and (d) 20 kHz, respectively. In the simulations, the estimated K_{eff} distribution, which is obtained from eqn (12), is used.

using the $K_{eff}(d_c^j)$ distribution. As shown, simulation results agree well with the experimental ones. The same applies to the other samples as shown in Fig. S9–S11. These results indicate that size-dependent anisotropy, *i.e.*, $K_{eff}(d_c)$, needs to be taken into account, while the K_{eff} distribution for each d_c does not need to be considered.

Discussion

Variation of K_{eff} with d_c in MNP samples

Fig. 4 presents the variation of the anisotropy constant as a function of d_c, $K_{eff}(d_c)$, and volume-weighted number density of the MNPs having d_c, $n_{d_c,V}(d_c)$ for the 4 samples examined. $K_{eff}(d_c)$ is calculated using eqn (12), while $n_{d_c,V}(d_c)$ is estimated from the static M–H curve. As shown in Fig. 4, overall, $K_{eff}(d_c)$ tends to decrease with increasing d_c. A similar trend was observed in previous studies.[30–32] Single-core samples, *i.e.*, SHP-15, SHP-20, and SHP-25, however, exhibit a distinct trend: when d_c exceeds the main core sizes d_{c_main} (approximately 15 nm, 20 nm, and 20 nm for SHP-15, SHP-20, and SHP-25, respectively), $K_{eff}(d_c)$ first steeply increases and then slowly decreases with increasing d_c. Moreover, the value of $K_{eff}(d_c)$ around d_{c_main}, remains relatively stable and does not exhibit significant variation with d_c. The partial enlarged view in Fig. 4(a–d) around $d_c = d_{c\_main}$ is shown in Fig. S13.

On the other hand, in the case of the multi-core sample, *i.e.*, Resovist, two d_{c_main} values are observed. The MNPs with smaller d_{c_main} (approximately 8 nm) are primarily composed of single-core MNPs, while the larger d_{c_main} (approximately 23 nm) corresponds predominantly to multi-core MNPs.[33] As shown in Fig. 4(d), for Resovist, $K_{eff}(d_c)$ first increases and then decreases with increasing d_c around the larger d_{c_main}. This behaviour resembles that observed in SHP series when d_c exceeds d_{c_main}. Therefore, this behaviour in single-core

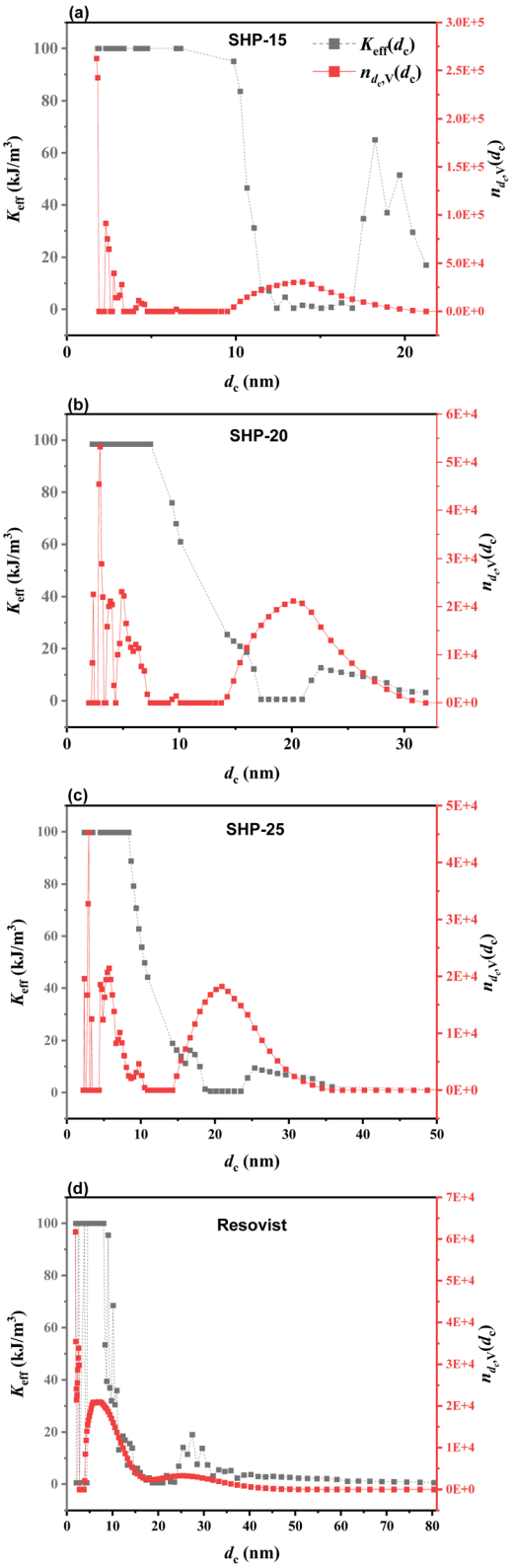

Fig. 4 Relationship between K_{eff} and d_c of 4 samples, which is obtained from eqn (12), and volume-weighted number density $n_{d_c,V}(d_c)$ of MNPs having d_c, which is obtained from the static M–H curve. (a)–(d) Correspond to the MNP samples SHP-15, SHP-20, SHP-25, and Resovist, respectively.

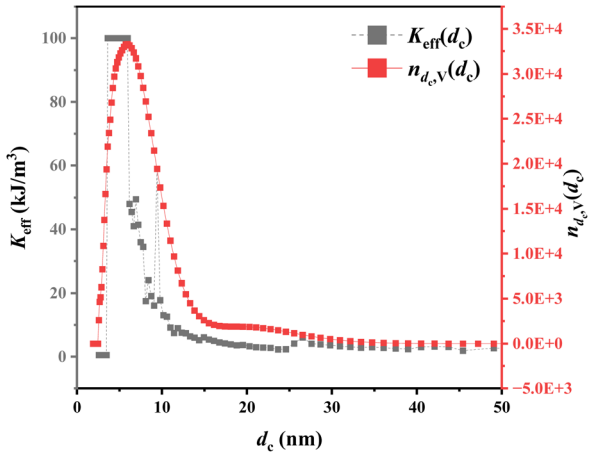

Fig. 5 Relationship between K_{eff} and d_c of MS3, which is obtained from eqn (12), and volume-weighted number density, $n_{d_c,V}(d_c)$, of MNPs having d_c, which is obtained from the static M–H curve.

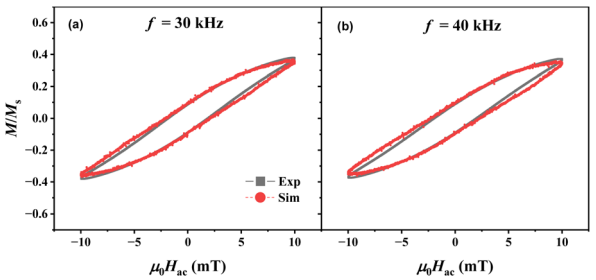

Fig. 6 Comparison between the experimental and simulation results of AC M–H for the SHP-20 sample under an excitation field amplitude of $\mu_0 H_{ac}$ = 10 mT and a frequency of (a) 30 kHz and (b) 40 kHz, respectively. In the simulations, the estimated K_{eff} distribution, which is obtained from eqn (12), is used.

samples (SHP-15, SHP-20, and SHP-25) will be due to the presence of multi-core MNPs when d_c exceeds the d_{c_main}. Note that the magnetization model that is used in the numerical simulation and estimation of K_{eff} distribution treats multi-core particles as an equivalent single-core particle,[26] thereby failing to capture the internal magnetic interactions within the multi-core. Consequently, the noticeable increase in $K_{eff}(d_c)$ is observed in each single-core sample when d_c exceeds the d_{c_main}. Such interactions to enhance the effective anisotropy constant K_{eff} have been reported in other studies.[34] Furthermore, similar trends have been reported in studies where the blocking temperature, which reflects the effective anisotropy energy barrier, varies with d_c and concentration due to dipolar interactions between MNPs.[35–38] In contrast, the constant behaviour of $K_{eff}(d_c)$ around d_{c_main} for SHP series reflects the characteristics of single-core particles.

As shown in Fig. 4, the values of $K_{eff}(d_c)$ for d_c < 10 nm reach the upper limit (100 kJ m^{-3}) for 4 samples. However, such high K_{eff} values for typical Fe_3O_4 and γ-Fe_2O_3 MNPs are unrealistic at room temperature.[39] This result may be attributed to two factors. First, for SHP series (*e.g.*, SHP-20), the MNPs with d_c < 10 nm do not exist. They are not observed in TEM (transmission electron microscopy) images (see Fig. S7). Therefore, the MNPs with d_c < 10 nm of SHP-20 observed by VSM is caused by the paramagnetic-like signal of SHP-20.[40,41] Second, for the Resovist sample, the MNPs with d_c < 10 nm have a small impact on the overall magnetic properties. Consequently, the accuracy of K_{eff} for d_c < 10 nm is low.

To confirm whether MNPs with d_c < 10 nm and K_{eff} = 100 kJ m^{-3} actually exist, we estimated $K_{eff}(d_c)$ of the MS3 sample using the same procedure as described above. Here, MS3 is a subset of the Resovist sample, in which particles larger than 20 nm were magnetically removed (see Fig. S3),[42] and the MNPs with d_c < 10 nm can be observed in the TEM image (see Fig. S5–S6). Fig. 5 shows the $K_{eff}(d_c)$ of the MS3 sample. As shown, K_{eff} for d_c of around 6–8 nm is approximately 15–60 kJ m^{-3}, which is much smaller than that of Resovist (K_{eff} is approximately within the range of 50 to 100 kJ m^{-3}). Therefore, extremely high K_{eff} for d_c < 10 nm observed in the Resovist sample does not reflect the actual physical properties, but rather results from the very small overall volume fraction of these particles.

Applicable excitation field range of estimated $K_{eff}(d_c)$

To verify whether the estimated $K_{eff}(d_c)$ obtained from the 1–20 kHz MPS data is applicable at higher frequencies, AC M–H curves of the SHP-20 sample were measured under the excitation field conditions of $\mu_0 H_{ac}$ = 10 mT with frequencies f = 30 kHz and 40 kHz and compared with the simulated curves using $K_{eff}(d_c)$. As shown in Fig. 6, the AC M–H curves obtained from simulations closely match the experiment data at a f of 30 kHz and 40 kHz. Similarly, good agreements are also obtained for the other samples as shown in Fig. S12. Moreover, the hysteresis loop area error between the experiment and the simulation is within 20 percent (Table S2). These results indicate that $K_{eff}(d_c)$, which is estimated using the 1–20 kHz MPS data, can be reliably used for f at least up to 40 kHz.

Conclusions

In this paper, we proposed a method to estimate an effective anisotropy constant K_{eff} distribution in a MNP sample. By using the estimated K_{eff} distribution in the simulation, AC M–H curves match the experiment results, demonstrating the effectiveness of the proposed method for both single-core and multi-core MNPs. Furthermore, our findings indicate that the K_{eff} distribution estimated from MPS data at f = 1–20 kHz, can be reliably used for simulations at frequencies up at least f = 40 kHz. This suggests that the frequency range of MPS measurements can be effectively extended through simulation by incorporating the K_{eff} distribution. We also discussed the variation of K_{eff} as a function of core size d_c in MNP samples, and demonstrated that K_{eff} varies depending on d_c and its formation of MNPs, *i.e.*, single-core or multi-core. The proposed method will be a reliable approach for an accurate estimation of K_{eff} distribution in a MNP sample and our findings provide deep insights for evaluating and optimising the MNP sample for various biomedical applications utilizing AC magnetization of MNPs.

Author contributions

Haochen Zhang: methodology, writing – original draft; Yi Sun: data curation; Haozhe Wang: visualization; Zhongzhou Du: editing, validation; Teruyoshi Sasayama: instrumentation design, writing – review & editing; Takashi Yoshida: writing – review & editing, conceptualization, supervision, funding acquisition.

Conflicts of interest

There are no conflicts to declare.

Data availability

The data that support the findings of this study are available on request from the corresponding author (e-mail: zhang.haochen.048@s.kyushuu.ac.jp), upon reasonable request.

Supplementary information (SI): experimental and simulation data supporting the findings of this study. It contains MPS (magnetic particle spectroscopy) data, VSM (vibrating sample magnetometry) data, DLS (dynamic light scattering) data, TEM figures, and numerical simulation results related to the magnetization behavior of the MNP samples. See DOI: **https://doi.org/10.1039/d5na00654f**.

Acknowledgements

This work was supported in part by the JSPS KAKENHI (Grant numbers JP23K17750 and JP25K01243). The authors gratefully acknowledge the use of the transmission electron microscopy facilities at the Ultramicroscopy Research Center (URC), Kyushu University.

References

1 B. Gleich and J. Weizenecker, *Nature*, 2005, **435**, 1214–1217.
2 S. Bai, T. Li, K. Li, L. Gai, Z. Du, C. Du, W. Zhang, T. Yoshdia and Y. Gu, *IEEE Trans. Magn.*, 2023, **59**, 1–5.
3 O. Ihab M, V. Narayanaswamy, S. Alaabed, S. Sambasivam and C. V. V. Muralee Gopi, *Magnetochemistry*, 2019, **5**, 67.
4 B. Rezaei, P. Yari, S. M. Sanders, H. Wang, V. K. Chugh, S. Liang, S. Mostufa, K. Xu, J.-P. Wang, J. Gómez-Pastora and K. Wu, *Small*, 2024, **20**, 2304848.
5 M. Graeser, F. Thieben, P. Szwargulski, F. Werner, N. Gdaniec, M. Boberg, F. Griese, M. Möddel, P. Ludewig, D. van de Ven, O. M. Weber, O. Woywode, B. Gleich and T. Knopp, *Nat. Commun.*, 2019, **10**, 1936.
6 J. Zhong, M. Schilling and F. Ludwig, *J. Phys. D: Appl. Phys.*, 2017, **51**, 015001.
7 Y. Ha, S. Ko, I. Kim, Y. Huang, K. Mohanty, C. Huh and J. A. Maynard, *ACS Appl. Nano Mater.*, 2018, **1**, 512–521.
8 C. C. Wu, L. Y. Lin, L. C. Lin, H. C. Huang, Y. F. Yang, Y. B. Liu, M. C. Tsai, Y. L. Gao, W. C. Wang, S. W. Hung, S. Y. Yang, H. E. Horng, H. C. Yang, W. Y. I. Tseng, H. I. Yeh, C. F. Hsuan, T. L. Lee and W. K. Tseng, *Appl. Phys. Lett.*, 2008, **92**, 142504.
9 Z. Xi, R. Huang, Z. Li, N. He, T. Wang, E. Su and Y. Deng, *ACS Appl. Mater. Interfaces*, 2015, **7**, 11215–11223.
10 K. Wu, J. Liu, R. Saha, D. Su, V. D. Krishna, M. C.-J. Cheeran and J.-P. Wang, *ACS Appl. Mater. Interfaces*, 2020, **12**, 13686–13697.
11 J. Zhong, E. L. Rösch, T. Viereck, M. Schilling and F. Ludwig, *ACS Sens.*, 2021, **6**, 976–984.
12 Y. Sun, N. Ye, D. Wang, Z. Du, S. Bai and T. Yoshida, *Nanomaterials*, 2020, **10**, 1623.
13 W. T. Coffey and Y. P. Kalmykov, J. T. Waldron, *The Langevin Equation*, World Scientific, 1996, vol. 95.
14 H. Risken, *The Fokker–Planck Equation*, 1996, vol. 18, 978-3-540-61530-9.
15 V. Schaller, G. Wahnström, A. Sanz-Velasco, P. Enoksson and C. Johansson, *J. Magn. Magn. Mater.*, 2009, **10**, 321.
16 K. Enpuku, A. L. Elrefai, J. Gotou, S. Yamamura, T. Sasayama and T. Yoshida, *J. Appl. Phys.*, 2021, **130**, 113903.
17 S. A. Shah, D. B. Reeves, R. M Ferguson, J. B. Weaver and K. M. Krishnan, *Phys. Rev. B*, 2015, **92**, 094438.
18 F. Ludwig, C. Balceris, T. Viereck, O. Posth, U. Steinhoff, H. Gavilan, R. Costo, L. Zeng, E. Olsson, C. Jonasson and C. Johansson, *J. Magn. Magn. Mater.*, 2017, **427**, 19–24.
19 K. Enpuku, S. Draack, F. Ludwig and T. Yoshida, *J. Appl. Phys.*, 2021, **130**, 183901.
20 T. Kahmann, E. Laureen Rösch, K. Enpuku, T. Yoshida and F. Ludwig, *J. Magn. Magn. Mater.*, 2021, **519**, 167402.
21 J. Garcia-Otero, A. J. Garcia-Bastida and J. Rivas, *J. Magn. Magn. Mater.*, 1998, **189**, 377.
22 S. Yoon and K. M. Krishnan, *J. Appl. Phys.*, 2011, **109**(7), 07B534.
23 I. J. Bruvera, P. Mendoza Zélis, M. Pilar Calatayud, G. F. Goya and F. H. Sánchez, *J. Appl. Phys.*, 2015, **118**(18), 184304.
24 D. Eberbeck, F. Wiekhorst, U. Steinhoff and L. Trahms, *J. Phys.: Condens. Matter*, 2006, **18**, S2829.
25 F. Ludwig, E. Heim, M. Schilling and K. Enpuku, *J. Appl. Phys.*, 2008, **103**, 07A314.
26 K. Enpuku, A. Elrefai, T. Yoshida, T. Kahmann, J. Zhong, T. Viereck and F. Ludwig, *J. Appl. Phys.*, 2020, **127**, 133903.
27 T. Sasayama, T. Yoshida and K. Enpuku, *Jpn. J. Appl. Phys.*, 2017, **56**, 025001.
28 T. Yoshida, S. Bai, A. Hirokawa, K. Tanabe and K. Enpuku, *J. Magn. Magn. Mater.*, 2015, **380**, 105–110.
29 H. Zhang, Y. Sun, Z. Du, T. Sasayama and T. Yoshida, *IEEE Magn. Lett.*, 2022, **14**, 1–4.
30 J. Mohapatra, F. Zeng, K. Elkins, M. Xing, M. Ghimire, S. Yoon, S. R. Mishra, J. P. Liu and J. P, *Phys. Chem. Chem. Phys.*, 2018, **20**(18), 12879–12887.
31 K. L. Pisane, S. Singh and M. S. Seehra, *Appl. Phys. Lett.*, 2017, **110**(22), 222409.
32 A. Demortière, P. Panissod, B. P. Pichon, G. Pourroy, D. Guillon, B. Donnio and S. Bégin-Colin, *Nanoscale*, 2011, **3**(1), 225.
33 A. Elrefai, T. Yoshida and K. Enpuku, *J. Magn. Magn. Mater.*, 2019, **474**, 522–527.
34 P. García-Acevedo, M. A. González-Gómez, Á. Arnosa-Prieto, L. de Castro-Alves, Y. Piñeiro and J. Rivas, *Adv. Sci.*, 2023, **10**, 2203397.

35 J. Dai, J.-Q. Wang, C. Sangregorio, J. Fang, E. Carpenter and J. Tang, *J. Appl. Phys.*, 2000, **87**, 7397–7399.
36 J. M. Vargas, W. C. Nunes, L. M. Socolovsky, M. Knobel and D. Zanchet, *Phys. Rev. B*, 2005, **72**, 184428.
37 W. C. Nunes, F. Cebollada, M. Knobel and D. Zanchet, *J. Appl. Phys.*, 2006, **99**, 08N705.
38 A. Z. Abbasi, C. L. Dennis, U. Rahman, M. Moroz, M. Jackson, M. F. Gillan, M. J. Allen and A. C. Nacev, *J. Phys. Chem. C*, 2011, **115**, 6257–6264.
39 G. Kresse and J. Hafner, *Phys. Rev. B:Condens. Matter Mater. Phys.*, 1997, **47**, 558–561.
40 D. Eberbeck, C. L. Dennis, N. F. Huls, K. L. Krycka, C. Gruttner and F. Westphal, *IEEE Trans. Magn.*, 2013, **49**, 269–274.
41 G. F. Goya, T. S. Berquó, F. C. Fonseca and M. P. Morales, *J. Appl. Phys.*, 2003, **94**(5), 3520–3528.
42 T. Yoshida, N. B. Othman and K. Enpuku, *J. Appl. Phys.*, 2013, **114**(17), 173908.